Nanoscale Horizons

ROYAL SOCIETY OF CHEMISTRY

COMMUNICATION

View Article Online
View Journal | View Issue

Cite this: *Nanoscale Horiz.*, 2023, 8, 1073

Received 31st March 2023,
Accepted 12th June 2023

DOI: 10.1039/d3nh00122a

rsc.li/nanoscale-horizons

Improving the efficiency of ternary organic solar cells by reducing energy loss†

Mengni Wang,[abc] Yanan Shi,[ab] Ziqi Zhang,[ab] Yifan Shen,[ab] Min Lv,[ab] Yangjun Yan,[d] Huiqion Zhou,[ab] Jianqi Zhang,[ab] Kun Lv,[ab] Yajie Zhang,*[ab] Hailin Peng[e] and Zhixiang Wei*[ab]

Effectively reducing the voltage loss in organic solar cells (OSCs) is critical to improving the power conversion efficiency (PCE) of OSCs. In this study, highly efficient ternary OSCs were constructed by adding a non-fullerene acceptor Qx2 with a high open-circuit voltage (V_{OC}) and low energy loss (E_{loss}) into PM6:m-BTP-PhC6 based binary devices. The third component Qx2 shows slightly complementary absorption with m-BTP-PhC6 and also optimizes the molecular packing, orientation, and morphology of the active layer. Moreover, the incorporation of Qx2 reduced the energetic disorder and improved the electroluminescence quantum efficiency, which suppresses the E_{loss} and further leads to a higher V_{OC} than the PM6:m-BTP-PhC6 binary blend. Consequently, synergetic enhancements of V_{OC}, short circuit current (J_{SC}), and fill factor (FF) are realized, resulting in the PCE of 18.60%. This work shows that the selection of the appropriate third component has positive implications for reducing E_{loss} and improving the PCE of OSCs.

New concepts

Compared with inorganic or perovskite solar cells, the open-circuit voltage (V_{OC}) of OSCs is still low, owing to the relatively large energy loss (E_{loss}). It is necessary to effectively reduce E_{loss} to further improve the PCE of OSCs. Previously reported work has focused on molecule design to improve the electroluminescence yield or reduce the reorganization energies to reduce non-radiative E_{loss}. However, it could hardly simultaneously improve all photovoltaic characters. We present a straightforward strategy to construct high-efficiency ternary OSCs with low E_{loss} by incorporating a high V_{OC} and low E_{loss} small molecule acceptor Qx2 into the PM6:m-BTP-PhC6 blend. The best PCE of 18.60% was achieved in the optimal ternary devices due to the synergistic enhancement of V_{OC} of 0.871 V, J_{SC} of 26.71 mA cm^{-2}, and FF of 80.04%. The optimal ternary devices based on PM6:m-BTP-PhC6:Qx2 achieved a higher electroluminescence yield value than that of binary devices based on PM6:m-BTP-PhC6, corresponding to a lower non-radiative energy loss (ΔE_3) and a higher V_{OC}. This work demonstrated that the appropriate selection of the third component not only reduces the nonradiative energy loss of the device, further increasing V_{OC}, but also realizes the simultaneous increase of J_{SC} and FF.

Introduction

Organic solar cells (OSCs) have attracted continuous attention as a promising clean energy technology due to their advantages of tunable molecular structures, solution processability, flexibility, lightweight properties, and low-cost large-area fabrication techniques.[1–9] Benefiting from the most advanced non-fullerene acceptors, precise morphology manipulation, and interface engineering, the power conversion efficiency (PCE) of OSCs has exceeded 19% with the best fill factors (FF) over 80%, showing their promising application prospects.[10–13]

The ternary blend strategy has been widely used as a practical and straightforward approach to improve the efficiency of OSCs.[14–16] By incorporating a third component, the light-harvesting of blend films could be improved, effectively promoting the short-circuit current density (J_{SC}).[17–19] Since most advanced non-fullerene acceptors possess favorable light-harvesting capabilities, the scope for further improvement of the J_{SC} is limited. Meanwhile, the open-circuit voltage (V_{OC}) of the OSCs is mostly lower than 0.9 V, which is much lower than the V_{OC} of perovskite and GaAs solar cells.[20] The unsatisfactory V_{OC} could be attributed to relatively large energy loss (E_{loss}). Compared with other high-efficiency solar cells, for instance, the GaAs solar cell has an E_{loss} of 0.29 eV and perovskite solar cells have an E_{loss} as low as 0.34 eV,[21,22] most of the advanced OSCs still possess a large E_{loss} of higher than 0.5 eV,[23,24] which shows a noticeable distance from the theoretical

[a] *Chinese Academy of Sciences (CAS) key laboratory of nanosystem and hierarchical fabrication, National Center for Nanoscience and Technology, Beijing 100190, China. E-mail: zhangyj@nanoctr.cn, weizx@nanoctr.cn*
[b] *University of Chinese Academy of Sciences, Beijing 100049, China*
[c] *Academy for Advanced Interdisciplinary Studies, Peking University, Beijing 100871, People's Republic of China*
[d] *School of Science, Beijing Jiaotong University, Beijing 100044, China*
[e] *Center for Nanochemistry, Beijing Science and Engineering Center for Nanocarbons, Beijing National Laboratory for Molecular Sciences, College of Chemistry and Molecular Engineering, Peking University, Beijing 100871, China. E-mail: hlpeng@pku.edu.cn*

† Electronic supplementary information (ESI) available. See DOI: https://doi.org/10.1039/d3nh00122a

value of 0.25–0.30 eV derived from the Shockley–Queisser (SQ) limit.[25] Therefore, suppressing the E_{loss} of OSC is the key to achieving higher V_{OC} as well as further improving PCE.

With the "tilted" orientation of the hexyl chains relative to the molecular plane, m-BTP-PhC6 is an outstanding non-fullerene acceptor material that exhibits more ordered intermolecular packing, resulting in enhanced electron mobility and good efficiency.[5] However, the relatively large energy loss of PM6:m-BTP-PhC6 based OSCs results in a non-ideal V_{OC}. Compared to the structure of m-BTP-PhC6, Qx2 has a different molecular backbone and side chains. The introduction of Qx2 could form a slightly complementary absorption spectrum with the PM6:m-BTP-PhC6 blend. Moreover, although QX2 has a similar lowest unoccupied molecular orbital (LUMO) energy level to m-BTP-PhC6, the PM6:Qx2 based OSCs possessed a much higher V_{OC} with an E_{loss} of less than 0.5 eV. Therefore, it is highly expected that Qx2 is a suitable third component for PM6:m-BTP-PhC6 based OSCs to increase the V_{OC} and J_{SC} simultaneously due to the lower E_{loss} of PM6:Qx2 binary devices.

In this contribution, we construct high-efficiency ternary OSCs with suppressed E_{loss} by incorporating the small molecule acceptor Qx2 into the PM6:m-BTP-PhC6 blends. The contact angle measurement confirmed that Qx2 is mainly located at the interface of PM6 and m-BTP-PhC6 as additional charge transport channels, leading to an ideal active layer morphology. The best PCE of 18.60% was achieved in the optimal ternary devices due to the synergistic enhancement of J_{SC} of 26.71 mA cm^{-2}, V_{OC} of 0.871 V, and FF of 80.04%. The J_{SC} improvement may be ascribed to the complementary absorption of m-BTP-PhC6 and Qx2, higher exciton dissociation probability, and suppressed recombination in the ternary blends. The increased FF is ascribed to the more balanced and efficient charge transport. The PM6:m-BTP-PhC6:Qx2 (1 : 0.98 : 0.42) based ternary devices gained a higher electroluminescence yield value of 1.94×10^{-4} than PM6:m-BTP-PhC6 based binary devices, corresponding to a decreased nonradiative energy loss (ΔE_3) of 0.221 eV and a higher V_{OC}.

Results and discussion

Molecular characterization

The chemical structures of the polymer donor PM6, and the small molecular acceptors BTP-m-PhC6 and Qx2 are illustrated in Fig. 1a. The normalized UV-vis absorption of these three materials (Fig. 1b) shows that the absorption spectrum of Qx2 is slightly complementary to those of PM6 and BTP-m-PhC6, which enhances the photon harvesting of the ternary blend film in contrast to the PM6-based binary blend films. The energy levels of PM6, m-BTP-PhC6, and Qx2 are presented in Fig. 1c. The highest occupied molecular orbital (HOMO) energy of Qx2 is −5.54 eV, which is marginally higher than the HOMO of m-BTP-PhC6 (−5.59 eV).[5] The identical LUMO energies of Qx2 and m-BTP-PhC6 are all located at −3.86 eV.[26] Interestingly, with the weight content of Qx2 in the acceptor mixture increasing, V_{OC} shows a linear tendency to increase (Fig. 1d).

Photovoltaic characteristics

The conventional device structure of indium tin oxide (ITO)/poly(3,4-ethylenedioxythiophene) : poly(styrene sulfonate) (PEDOT :

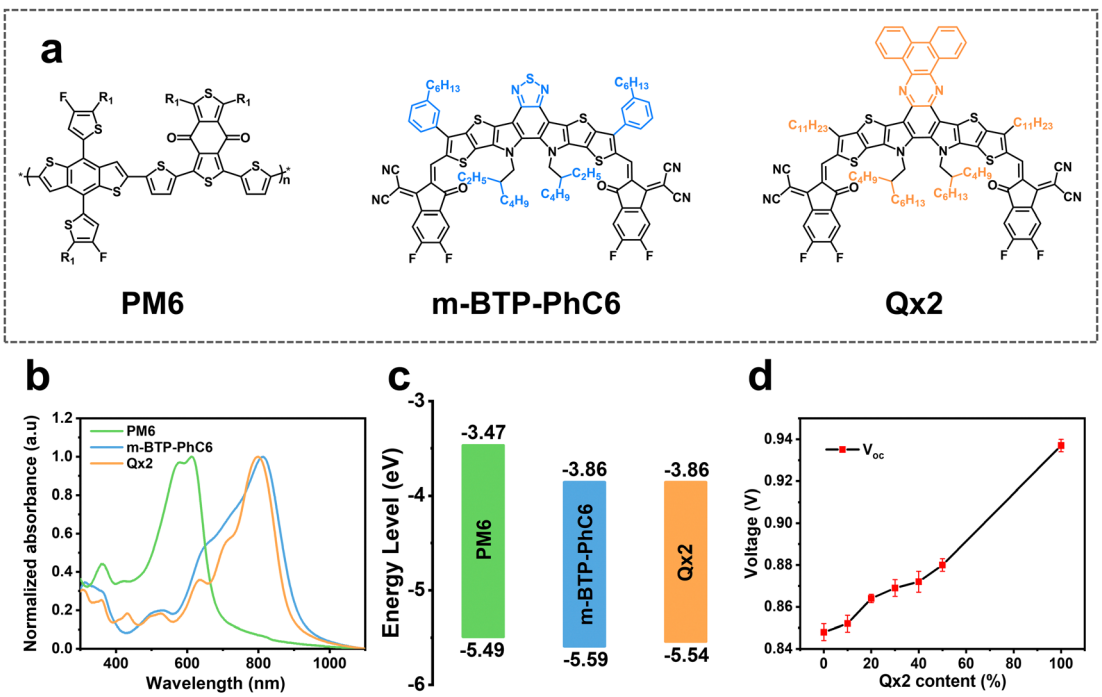

Fig. 1 (a) Chemical structures and (b) normalized UV-vis spectra of PM6, m-BTP-PhC6 and Qx2 thin films. (c) Energy level alignment diagram of the studied materials[5,26] (d) The change of the VOCs in ternary devices with different weight ratios of Qx2.

PSS)/active layer/PNDIT-F3N/Ag was utilized to fabricate OSCs for the evaluation of the photovoltaic performance. The donor and acceptor materials are dissolved in chloroform solution with 0.6 vol% 1-chloronaphthalene as the solvent additive. Detailed fabrication methods are demonstrated in the ESI.† Fig. 2a shows the representative current–voltage (*J*–*V*) characteristics of the optimized binary and ternary OSCs measured under simulated AM1.5G sun illumination (100 mW cm^{-2}) and the corresponding photovoltaic characters are summarized in Table 1. For PM6:m-BTP-PhC6 binary OSCs, the best performance indicates a PCE of 17.12%, with a V_{OC} of 0.850 V, a J_{SC} of 25.69 mA cm^{-2}, and an FF of 78.43%. Using PM6:Qx2 as the active layer, the device delivers a PCE of 17.11%, with a higher V_{OC} of 0.935 V, a J_{SC} of 24.28 mA cm^{-2}, and an FF of 75.37%. With increasing Qx2 weight ratio in ternary blends, a linear increase in V_{OC} is observed (Fig. 1d), and the optimized PCE of ternary OSCs is achieved with a 30% Qx2 weight ratio. The champion ternary OSC exhibits an outstanding PCE of 17.97% with an enhanced V_{OC} of 0.875 V, a J_{SC} of 25.91 mA cm^{-2}, and an FF of 79.12%. When we used 2PACZ as the transport layer, the PCE was higher (18.62%), with an impressive J_{SC} of 26.71 mA cm^{-2} and an outstanding FF of over 80%. Compared with the PM6:m-BTP-PhC6 binary system, the distinctly improved V_{OC} does not sacrifice J_{SC} and FF. The *J*–*V* curve of ternary devices with different weight ratios Qx2 and corresponding photovoltaic characters are summarized in Table S1 and Fig. S1a (ESI†). Since the optimal ternary devices keep the donor : acceptor ratio of 1 : 1.4, we also used this ratio to construct binary devices to exclude the influence of the change of the donor : acceptor ratio on the device photovoltaic characters, and the corresponding results are in Table S2 (ESI†). The reproducibility of the optimized binary and ternary OSCs is also evaluated by the statistical distribution of efficiencies originating from 20 independent devices, as shown in Fig. 2b. The efficiencies of most optimized ternary devices are located around 17.8%, which confirms the effectiveness of this ternary strategy.

To investigate the internal causes of the J_{SC} increase, the external quantum efficiency (EQE) curves are plotted in Fig. 2c and Fig. S1b (ESI†). Though the inevitable spectrum mismatch and nonlinear photocurrent response to light intensity lead to a difference between the J_{SC} from EQE measurement and J_{SC} from the *J*–*V* curve, the integrated J_{SC} of the devices from the

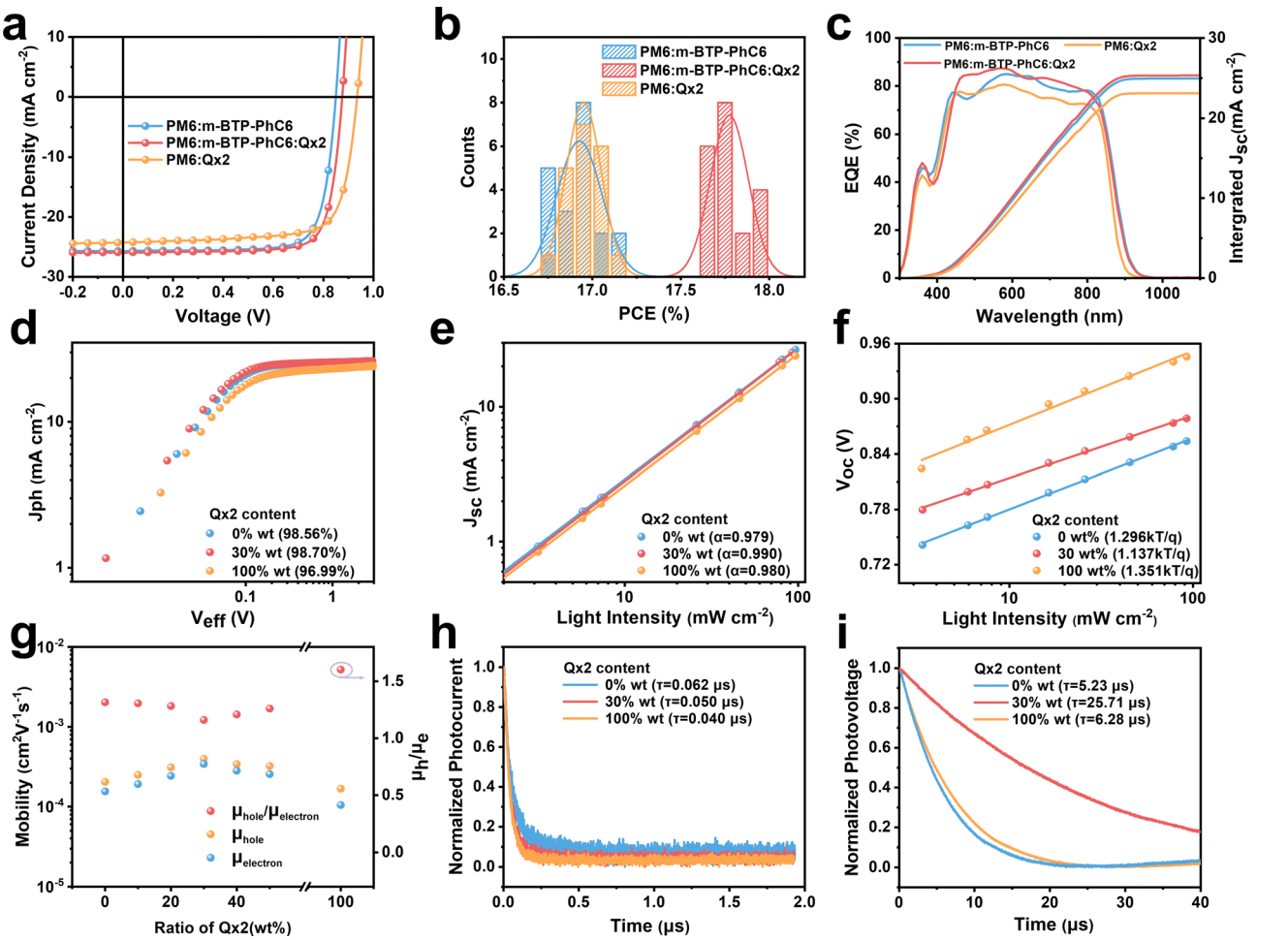

Fig. 2 (a) Characteristic *J*–*V* curves under simulated AM 1.5G irradiance (100 mW cm^{-2}). (b) Statistical PCE distribution of binary and optimized ternary devices. (c) The corresponding EQE spectra and integrated J_{SC}. (d) Photocurrent density (J_{ph}) *versus* effective bias (V_{eff}). The light-intensity-dependence of J_{SC} (e) and V_{OC} (f) of binary and optimized ternary devices. (g) Mobility of holes and electrons in binary and ternary devices with different Qx2 weight ratios. (h) TPC and (i) TPV curves of the binary and optimized ternary OSCs.

Table 1 Photovoltaic characters of binary and optimized ternary OSCs

Active layer combinations	Qx2 content [%]	V_{OC} (V)	J_{SC} (mA cm^{-2})	Fill factor (%)	Efficiency[a] (%)
PM6:m-BTP-PhC6	0	0.850 (0.848 ± 0.004)	25.69 (25.48 ± 0.23)	78.43 (78.37 ± 0.40)	17.12 (16.92 ± 0.12)
PM6:m-BTP-PhC6:Qx2	30	0.875 (0.869 ± 0.004)	25.91 (25.96 ± 0.26)	79.12 (78.76 ± 0.72)	17.97 (17.77 ± 0.10)
	30[b]	0.871 (0.866 ± 0.006)	26.71 (26.77 ± 0.14)	80.04 (79.21 ± 0.87)	18.62 (18.35 ± 0.17)
PM6:Qx2	100	0.935 (0.937 ± 0.003)	24.28 (24.34 ± 0.25)	75.37 (74.29 ± 0.79)	17.11 (16.95 ± 0.10)

[a] The average values with standard deviation were obtained from at least 10 individual devices. [b] The ternary devices utilize 2PACZ as the transport layer.

EQE spectra matched well with the J_{SC} from the J–V curve with errors less than 5%. The introduction of Qx2 leads to a slight blue-shift in absorption edge, but higher ternary EQE values over almost the entire absorption range (450–800 nm).

The behavior of the exciton dissociation as well as the charge recombination mechanism were also analyzed. Various relevant measurements were performed, including the dependence of photocurrent density (J_{ph}) extraction on the applied electric field and the dependence of J_{SC} and V_{OC} on the light intensity. The J_{ph} is the difference between J_L and J_D, where the J_L represents the light current density and the J_D represents the dark current density. V_{eff} is the difference between V_0 (the voltage when J_{ph} = 0) and V (the applied bias). Firstly, with the $V_{eff} > 2$ V, the J_{ph} of all devices approached saturation (J_{sat}), which means complete dissociation and charge collection. We utilize the ratio of J_{ph}/J_{sat} to evaluate the exciton dissociation probability ($P(E, T)$).[27] As shown in Fig. 2d, for the optimized PM6:m-BTP-PhC6 binary and PM6:m-BTP-PhC6:Qx2 ternary device, $P(E, T)$ is 0.9856 and 0.9870, respectively. It turns out that ideal exciton dissociation results in high J_{SC} and FF.[28] Furthermore, the power law relationship between J_{SC} and the light intensity (P_{light}) can be characterized as $J_{SC} \propto (P_{light})^{\alpha}$, where α is the exponential factor describing the degree of charge recombination (Fig. 2e).[29] Compared to the α value of the binary devices (0.979 and 0.980), the α value of the PM6:m-BTP-PhC6:Qx2 ternary device (0.990) is improved, demonstrating more efficient free charge collection with less biomolecular recombination within the PM6:m-BTP-PhC6:Qx2 devices.

As shown in Fig. 2f, the relationship of V_{OC} dependence on P_{light} can be fitted by $V_{OC} \propto n(kT/q) \ln P_{light}$, where k is the Boltzmann constant, T is the absolute temperature, and q is the elemental charge. The n value is utilized to evaluate the degree of trap-assisted recombination.[30] The closer n is to 1, the more trap-assisted recombination is suppressed. Accordingly, the n values for PM6:m-BTP-PhC6, PM6:m-BTP-PhC6:Qx2, and PM6:Qx2 devices turn out to be 1.296, 1.137, and 1.351, respectively, demonstrating that the addition of Qx2 can effectively prevent the trap-assisted recombination in devices.[31] And it could also be verified by the enhanced FF. Further detailed J_{ph}–V_{eff} curves, and the dependence of J_{SC} and V_{OC} on the light intensity of the two binary and ternary OSCs, are presented in Fig. S2 (ESI†).

To investigate the dynamic charge transport process in the active layers, the space-charge limited current (SCLC) method was performed to measure the carrier mobilities. Fig. 2g and Table S3 (ESI†) show the hole mobility (μ_h) and electron mobility (μ_e) obtained by fitting the curves. In comparison with the two binary blends, both μ_h and μ_e of the ternary blends are increased, indicating a more balanced charge transport. Transient photocurrent (TPC) and transient photovoltage (TPV) measurements were also performed (Fig. 2h and i) to further explore the charge transport process. The photocurrent of the ternary device decays faster than that in the PM6:m-BTP-PhC6 device, indicating that the trap-state density of the ternary device is lower than that in the PM6:m-PhC6 based device.[32] The reduced trap state density is one of the reasons that the trap-assisted recombination of the ternary device is inhibited after the incorporation of Qx2. Moreover, the charge extraction time of ternary OSCs (0.050 μs) is shorter than that of PM6:m-BTP-PhC6 based binary devices (0.062 μs). Likewise, the carrier lifetimes are 5.23 μs, 25.71 μs, and 6.28 μs for PM6:m-BTP-PhC6, PM6:m-BTP-PhC6:Qx2, and PM6:Qx2 OSCs, respectively. The reduced charge extraction time and increased carrier lifetime of the ternary OSCs are conducive to increased charge mobility and inhibited charge combination, which contributes to the improvement of J_{SC} and FF.[33–35]

Energy loss

To reveal the underlying cause of the increase in V_{OC}, we investigated the energy loss ($E_{loss} = E_g - qV_{OC}$, where E_g is the bandgap) (Fig. 3a–c) of the devices, which can be quantified as the following equation:[36]

$$\begin{aligned} E_{loss} = E_g - qV_{OC} &= \left(E_g - qV_{OC}^{SQ}\right) + \left(qV_{OC}^{SQ} - qV_{OC}^{rad}\right) + \left(qV_{OC}^{rad} - qV_{OC}\right) \\ &= \left(E_g - qV_{OC}^{SQ}\right) + q\Delta V_{OC}^{rad,belowgap} + qV_{OC}^{non\text{-}rad} \\ &= \Delta E_1 + \Delta E_2 + \Delta E_3 \end{aligned} \quad (1)$$

where V_{OC}^{SQ} is the maximum V_{OC} predicted by the SQ limit, and V_{OC}^{rad} is the V_{OC} when only radiative recombination is present in the devices. We performed the Fourier transform photocurrent spectroscopy (FTPS)-EQE measurement and took the derivative of the curve to determine the E_g values:[37]

$$E_g = \frac{\int_a^b E_g P(E_g) \mathrm{d}E_g}{\int_a^b P(E_g) \mathrm{d}E_g} \quad (2)$$

where the selection basis of the integral boundary a and b is that $P(a) = P(b) = 0.5\mathrm{Max}[P(E_g)]$.

In eqn (1), ΔE_1 originated from the mismatch between solid angle solar irradiation and omnidirectional blackbody radiation of the absorption above the optical gap. Therefore, ΔE_1 is inevitable once the E_g is confirmed.[38] ΔE_2 is due to the radiative

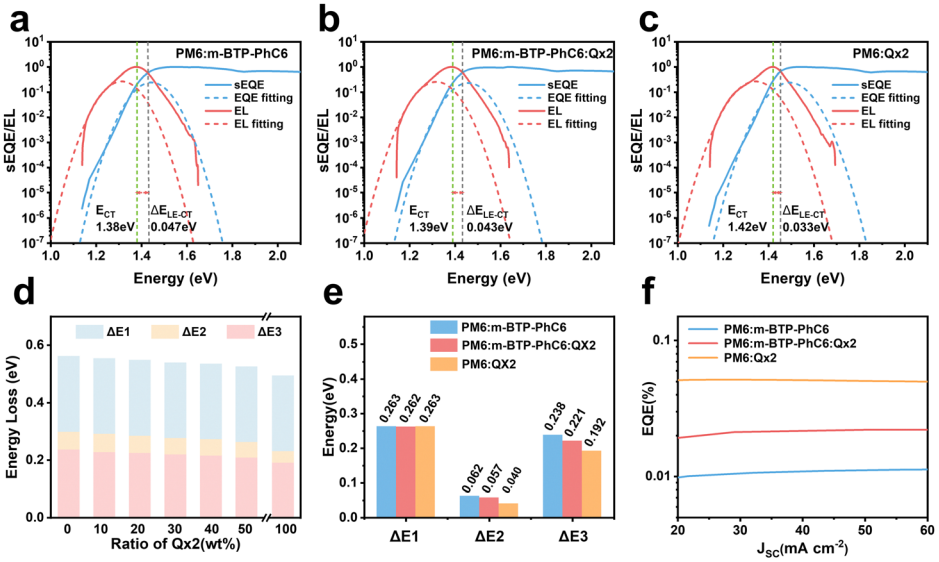

Fig. 3 Normalized FTPS-EQE and EL curves with Gaussian fits using the Marcus equation for (a) PM6:m-BTP-PhC6, (b) PM6:m-BTP-PhC6:Qx2, and (c) PM6:Qx2-based devices. (d) Variation tendency in energy loss of binary and ternary devices with different Qx2 ratios. (e) Statistical diagram of energy loss. (f) EQE_{EL} curves of the binary and optimized ternary devices.

recombination below the bandgap of the active layer in bulk heterojunction OSCs, which is partly associated with the reorganization energy and the energetic disorder degree of the blends.[37] ΔE_3 is attributed to the nonradiative recombination at the donor/acceptor interfaces in OSCs, which can be calculated from:[36]

$$\Delta E_3 = kT\ln(\mathrm{EQE_{EL}}) \quad (3)$$

where k is the Boltzmann constant, T is the Kelvin temperature, and EQE_{EL} is the device's electroluminescence quantum efficiency.

The bandgaps are calculated as 1.419 eV for the PM6:m-BTP-PhC6 binary blend, 1.420 eV for the optimized PM6:m-BTP-PhC6:Qx2 ternary blend, and 1.427 eV for the PM6:Qx2 binary blend. More detailed information on the E_{loss} is shown in Table 2 and Table S4 (ESI†). As shown in Fig. 3d, the energy loss shows a decreasing trend with increasing Qx2 content. E_{loss} of the optimized ternary device is 0.539 eV, lower than that of the PM6:m-BTP-PhC6 based device (0.560 eV). Profiting from the introduction of Qx2, the differences in energy loss principally originate from the decrease of ΔE_2 and ΔE_3, which can be attributed to the sharp absorption edge and the suppressive nonradiative recombination (Fig. 3e).

As discussed in dedicated studies, active layer absorption edge and nonradiative recombination are related to the energetic disorder. We evaluated the degree of the energetic disorder in terms of an Urbach energy parameter (E_U), which follows Urbach's rule:[39]

$$\alpha(E) = \alpha_0 e^{(E-E_g)/E_U} \quad (4)$$

where $\alpha(E)$ is the absorption coefficient, E is the photon energy, α_0 (absorption coefficient at the bandgap) and E_g are two constants. The smaller E_U is, the lower the energetic disorder is, and *vice versa*. By fitting the FTPS-EQE curves, the E_U values are 24.56 meV for the PM6:m-BTP-PhC6 binary device, 23.61 meV for the optimized ternary device, and 23.17 meV for the PM6:Qx2 binary device (Fig. S3, ESI†). The variation tendency of E_U is consistent well with the reduction of ΔE_2 as well as the more abrupt EQE edges, as mentioned above.

For further analysis of ΔE_3, we measured and contrasted the E_{CT} (energy of charge transfer states) and electroluminescence quantum efficiency of the two binary and optimized ternary devices.[18,19,40] E_{CT} could be obtained by Gaussian fitting of highly sensitive EQE and EL (electroluminescence) using Marcus equations:[41]

$$\mathrm{EQE_{PV}}(E) = \frac{f_j}{E\sqrt{4\pi\lambda_j kT}}\exp\left(\frac{-(E_{CT}+\lambda_j-E)^2}{4\lambda_j kT}\right) \quad (5)$$

$$\mathrm{EQE_{EL}}(E) = \frac{Ef_j}{\sqrt{4\pi\lambda_j kT}}\exp\left(\frac{-(E_{CT}-\lambda_j-E)^2}{4\lambda_j kT}\right) \quad (6)$$

where λ_j is the reorganization energy; f_j is the electronic

Table 2 Detailed information on energy losses of two binary and optimized ternary systems

Qx2 content [wt%]	E_g (eV)	qV_{OC} (eV)	qV_{OC}^{SQ} (eV)	qV_{OC}^{rad} (eV)	E_{loss} (eV)	ΔE_1	ΔE_2	ΔE_3	EQE_{EL}
0	1.419	0.859	1.156	1.094	0.560	0.263	0.062	0.238	1.00E-4
30	1.420	0.881	1.157	1.100	0.539	0.262	0.057	0.221	1.94E-4
100	1.427	0.934	1.164	1.124	0.493	0.263	0.040	0.192	5.95E-4

coupling (transfer integral) between states. As shown in Fig. 3a–c, the results of Gaussian fits demonstrated that the E_{CT} is 1.38 eV for PM6:m-BTP-PhC6, 1.39 eV for PM6:m-BTP- PhC6:Qx2 and 1.42 eV for PM6:Qx2 based devices, respectively.[40] And $\Delta E_{LE\text{-}CT}$ (the energy difference between the lowest singlet or triplet excited state and the charge transfer state) for the PM6:m-BTP-PhC6, PM6:m-BTP-PhC6:Qx2, and PM6:Qx2 based devices is calculated to be around 0.047 eV, 0.043 eV, and 0.033 eV, respectively. The decreased $\Delta E_{LE\text{-}CT}$ is beneficial in reducing the probability of nonradiative relaxation, which partly mitigates the nonradiative recombination.[42,43]

The results of the EQE_{EL} measurement are presented in Fig. 3f and Table S4 (ESI†). The EQE_{EL} of the optimized ternary device is 1.94×10^{-4}, obviously higher than that of the PM6:m-BTP-PhC6 based binary device (1.00×10^{-4}), and thus the ΔE_3 of the optimized ternary device (0.221 eV) is lower than that of the binary device (0.238 eV). Accordingly, in comparison with the binary devices, the reduced ΔE_2 and ΔE_3 induced a suppressive total energy loss for PM6:m-BTP-PhC6:Qx2 based devices, which contributes to the increase of V_{OC}.

Film morphology

To study the effects of the third component Qx2 on the morphology of the blend films, the miscibility was checked by contact angle measurement. As the miscibility of Qx2 with PM6 and m-BTP-PhC6 largely determines the distribution of Qx2 in the active layer, this is closely associated with the device performance. The surface energies of the pristine PM6, m-BTP-PhC6, and Qx2 films are 14.11, 20.10, and 16.86 mN m^{-1}, respectively (Fig. 4 and Table S5, ESI†). Furthermore, the Flory-Huggins interaction parameter, which is calculated from the surface energy of a neat film, could be used to assess the degree of miscibility between the two molecules.[44] Smaller χ^{D-A} (the Flory–Huggins interaction parameter between the donor and acceptor) values correspond to better miscibility, and *vice versa*.[45,46] The χ^{D-A} value between PM6 and m-BTP-PhC6 turns out to be 0.53, much higher than the 0.12 between PM6 and Qx2, demonstrating the better miscibility between the two acceptors as well as the reduced mixing ability between PM6 and m-BTP-PhC6. With the incorporation of 30 wt% Qx2 into the film, the m-BTP-PhC6:Qx2 binary composite showed a reduced χ^{D-A} value of 0.30, certifying that Qx2 could be applicable to regulate the miscibility between PM6 and m-BTP-PhC6. To further confirm the thermodynamic position of the incorporated Qx2 in the ternary system (D: A_1: A_2), the wetting coefficient (ω) of the third ingredient A_2 in the blends of host D and A_1 was calculated by Young's equation:[30]

$$\omega_{A_2} = \frac{\gamma_{A_1/A_2} - \gamma_{D/A_2}}{\gamma_{D/A_1}} \quad (7)$$

where γ_{A_1/A_2} refers to the interfacial surface energy between A_1 and A_2, and can be further calculated by Wu's equation as follows:[47]

$$\gamma_{A_1/A_2} = \gamma_{A_1} + \gamma_{A_2} - 4\left(\frac{\gamma^d_{A_1}\gamma^d_{A_2}}{\gamma^d_{A_1} + \gamma^d_{A_2}} + \frac{\gamma^p_{A_1}\gamma^p_{A_2}}{\gamma^p_{A_1} + \gamma^p_{A_2}}\right) \quad (8)$$

where the γ^d_A and γ^p_A are the dispersive and polar components of γ_A.

For the PM6:m-BYP-PhC6:Qx2 ternary blend, the $\omega_{m\text{-}BTP\text{-}PhC6/Qx2}$ turns out to be 0.709, which is in the range of −1 and 1, implying that Qx2 is more inclined to locate at the interface between PM6 and m-BTP-PhC6. Therefore, the Qx2 introduction may promote molecular miscibility at the donor and acceptor interface, and this structure facilitates efficient separation and collection of charges, which benefits the J_{SC} increase.

Atomic force microscopy (AFM) and grazing incident wide-angle X-ray diffraction (GIWAX) measurements were performed to further verify the morphology of the active layers. From the AFM height images of the blend films shown in Fig. 5a, we find that all the blends contain similar fibrous structures. The PM6:m-BTP-PhC6 blend reveals a root-mean-square (RMS) surface roughness value of 1.09 nm. By contrast, the PM6:m-BTP-PhC6:Qx2 blend with 30.0 wt% Qx2 has a smoother surface (RMS = 0.968 nm) than those of the PM6:m-BTP-PhC6 and PM6:Qx2 binary blends (RMS = 1.09 nm and 1.03 nm, respectively). This demonstrates that the excessive aggregation of the two acceptors in the ternary blends could be suppressed due to the good compatibility between m-BTP-PhC6 and Qx2, thus

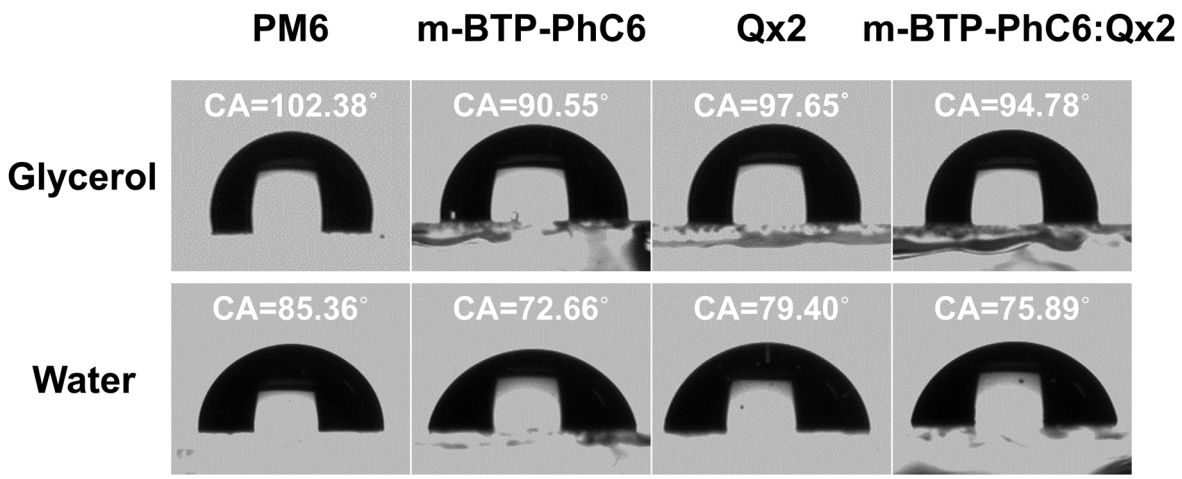

Fig. 4 Contact angle images of PM6, m-BTP-PhC6, m-BTP-PhC6:Qx2, Qx2 films with water and glycerol droplets.

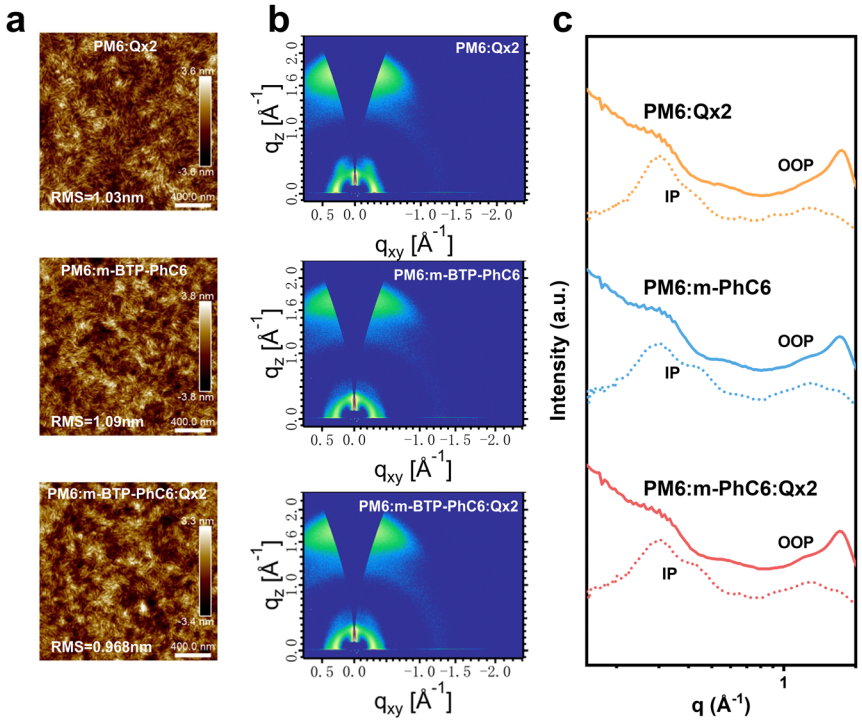

Fig. 5 (a) AFM height images of PM6:m-BTP-PhC6, PM6:m-BTP-PhC6:Qx2, and PM6:Qx2 blends. (b) 2D-GIWAXS patterns of PM6:m-BTP-PhC6, PM6:m-BTP-PhC6:Qx2, and PM6:Qx2 blend films. (c) Corresponding profile intensity in the in-plane and out-of-plane directions.

facilitating charge transport. GIWAXS analysis was also used to characterize the molecular packing of the active layers. Fig. 5b and c displays the two-dimensional GIWAXs (2D-GIWAXs) patterns and the corresponding in-plane (IP) and out-of-plane (OOP) intensity profiles of relevant binary and ternary blend films. By the evident lamellar stacking peaks in the IP-direction and π–π stacking peaks in the OOP direction, we confirmed that all the blended films are more inclined to face-on orientation, which improved the charge transfer capability in OSCs and indicated that the incorporation of Qx2 to construct ternary blended films has very little effect on the orientation of the molecules. The corresponding crystalline correlation lengths (CCL) correlated with the π–π stacking peaks in PM6:m-BTP-PhC6, PM6:Qx2, and ternary blends are 21.34 Å, 21.88 Å, and 21.62 Å, respectively. The CCL result indicates that the introduction of QX2 did not significantly affect the crystallinity of the ternary blend films and moderate domain sizes are conducive to charge transport and collection. The π–π stacking peaks in PM6:m-BTP-PhC6, PM6:Qx2, and ternary blends are 3.63 Å, 3.59 Å, and 3.65 Å, respectively. The increased π–π stacking distance in the ternary blends verifies the better miscibility at the interface of donor and acceptor phases.

Conclusion

In summary, high-performance ternary OSCs were realized by introducing a non-fullerene acceptor Qx2 with much lower energy loss into the PM6:m-BTP-PhC6 based OSCs, which achieves a synergistic improvement of J_{SC}, V_{OC}, and FF. The wetting coefficient value reveals that QX2 introduction not only has good compatibility with the m-BTP-PhC6 acceptor, but also promotes molecular miscibility at the donor and acceptor interface, which is conducive to exciton separation and charge transport and leads to an ideal morphology and molecular orientation in the ternary blend films. The increase in V_{OC} could be partly due to the lower ΔE_2 resulting from the decrease in energetic disorder. The reduced nonradiative recombination, which originates from the reduced $\Delta E_{LE\text{-}CT}$ and the higher electroluminescence quantum efficiency, contributed most of the reduced total energy loss. Therefore, the optimized PM6:m-BTP-PhC6:Qx2 ternary device, after incorporation of 30%wt Qx2, shows a best PCE of 18.62%, with a J_{SC} of 26.71mA cm^{-2}, a V_{OC} of 0.871 V, and an FF of 80.04%. This work demonstrated that the appropriate selection of the third component not only reduces the nonradiative energy loss of the device, further increasing V_{OC}, but also realizes the simultaneous increase of J_{SC} and FF.

Author contributions

Wang MN fabricated all the OSC devices, tested the device performance and wrote the original draft. Shi YN synthesized the small molecule acceptor Qx2. Zhang ZQ, Shen YF and Yan YJ helped the energy loss measurement. Lv M helped the contact angle measurement. Zhang JQ completed the GIWAXS measurement. Zhou HQ completed the TPC and TPV measurement. Zhang YJ and Wei ZX guided the idea and finalized the

manuscript. All authors participated in general discussion and the manuscript revision.

Conflicts of interest

The authors declare that they have no conflict of interest.

Acknowledgements

The authors acknowledge the financial support from the National Natural Science Foundation of China (Grant No. 21975059, 22135001, 21721002), the Strategic Priority Research Program of the Chinese Academy of Sciences (No. XDB36000000).

References

1 J. Zhang, S. Luo, H. Zhao, X. Xu, X. Zou, A. Shang, J. Liang, F. Bai, Y. Chen, K. S. Wong, Z. Ma, W. Ma, H. Hu, Y. Chen and H. Yan, *Angew. Chem., Int. Ed.*, 2022, **61**, e202206930.
2 J. Zhang, F. Bai, I. Angunawela, X. Xu, S. Luo, C. Li, G. Chai, H. Yu, Y. Chen, H. Hu, Z. Ma, H. Ade and H. Yan, *Adv. Energy Mater.*, 2021, **11**, 2102596.
3 J. X. Wang, C. Y. Han, J. H. Han, F. Z. Bi, X. K. Sun, S. G. Wen, C. P. Yang, C. M. Yang, X. C. Bao and J. H. Chu, *Adv. Energy Mater.*, 2022, **12**, 2201614.
4 X. Duan, W. Song, J. Qiao, X. Li, Y. Cai, H. Wu, J. Zhang, X. Hao, Z. Tang, Z. Ge, F. Huang and Y. Sun, *Energy Environ. Sci.*, 2022, **15**, 1563–1572.
5 G. Chai, Y. Chang, J. Zhang, X. Xu, L. Yu, X. Zou, X. Li, Y. Chen, S. Luo, B. Liu, F. Bai, Z. Luo, H. Yu, J. Liang, T. Liu, K. S. Wong, H. Zhou, Q. Peng and H. Yan, *Energy Environ. Sci.*, 2021, **14**, 3469–3479.
6 H. Lu, D. Li, G. Ran, Y.-N. Chen, W. Liu, H. Wang, S. Li, X. Wang, W. Zhang, Y. Liu, X. Xu and Z. Bo, *ACS Energy Lett.*, 2022, **7**, 3927–3935.
7 J. Li, Z. Zhang, G. Ran, X. Xu, C. E. Zhang, W. Liu, X. Zheng, D. Li, X. Xu, Y. Liu, Z. Tang, W. Zhang and Z. Bo, *Small*, 2022, **18**, 2203454.
8 J. Guo, X. Xia, B. Qiu, J. Zhang, S. Qin, X. Li, W. Lai, X. Lu, L. Meng, Z. Zhang and Y. Li, *Adv. Mater.*, 2023, 2211296.
9 H. Yang, W. Chen, Y. Yu, Y. Shen, H. Yang, X. Li, B. Zhang, H. Chen, Q. Cheng, Z. Zhang, W. Qin, J.-D. Chen, J.-X. Tang, Y. Li and Y. Li, *Adv. Mater.*, 2023, **35**, 2208604.
10 C. Li, J. Zhou, J. Song, J. Xu, H. Zhang, X. Zhang, J. Guo, L. Zhu, D. Wei, G. Han, J. Min, Y. Zhang, Z. Xie, Y. Yi, H. Yan, F. Gao, F. Liu and Y. Sun, *Nat. Energy*, 2021, **6**, 605–613.
11 S. Bao, H. Yang, H. Fan, J. Zhang, Z. Wei, C. Cui and Y. Li, *Adv. Mater.*, 2021, **33**, e2105301.
12 H. Wang, Y. Yang, Y. Zhang, S. Wang, Z. A. Tan, S. Yan, L. Wang, J. Hou and B. Xu, *Adv. Funct. Mater.*, 2023, **33**, 2213914.
13 H. Chen, S. Y. Jeong, J. Tian, Y. Zhang, D. R. Naphade, M. Alsufyani, W. Zhang, S. Griggs, H. Hu, S. Barlow, H. Y. Woo, S. R. Marder, T. D. Anthopoulos, I. McCulloch and Y. Lin, *Energy Environ. Sci.*, 2023, **16**, 1062–1070.
14 M. Zhang, L. Zhu, T. Hao, G. Zhou, C. Qiu, Z. Zhao, N. Hartmann, B. Xiao, Y. Zou, W. Feng, H. Zhu, M. Zhang, Y. Zhang, Y. Li, T. P. Russell and F. Liu, *Adv. Mater.*, 2021, **33**, 2007177.
15 N. Y. Doumon, L. Yang and F. Rosei, *Nano Energy*, 2022, **94**, 106915.
16 H. Lu, H. Wang, G. Ran, S. Li, J. Zhang, Y. Liu, W. Zhang, X. Xu and Z. Bo, *Adv. Funct. Mater.*, 2022, **32**, 2203193.
17 Y. Cai, C. Xie, Q. Li, C. Liu, J. Gao, M. H. Jee, J. Qiao, Y. Li, J. Song, X. Hao, H. Y. Woo, Z. Tang, Y. Zhou, C. Zhang, H. Huang and Y. Sun, *Adv. Mater.*, 2023, **35**, 2208165.
18 Y. Li, Y. Cai, Y. Xie, J. Song, H. Wu, Z. Tang, J. Zhang, F. Huang and Y. Sun, *Energy Environ. Sci.*, 2021, **14**, 5009–5016.
19 Y. Cai, Y. Li, R. Wang, H. Wu, Z. Chen, J. Zhang, Z. Ma, X. Hao, Y. Zhao, C. Zhang, F. Huang and Y. Sun, *Adv. Mater.*, 2021, **33**, e2101733.
20 G. Yang, H. Zhang, S. Li, Z. Ren, G. Fang, D. Lei and G. Li, *SmartMat*, 2022, **3**, 513–521.
21 Z. Liu, L. Krückemeier, B. Krogmeier, B. Klingebiel, J. A. Márquez, S. Levcenko, S. Öz, S. Mathur, U. Rau, T. Unold and T. Kirchartz, *ACS Energy Lett.*, 2019, **4**, 110–117.
22 M. A. Green and A. W. Y. Ho-Baillie, *ACS Energy Lett.*, 2019, **4**, 1639–1644.
23 P. Cheng, G. Li, X. Zhan and Y. Yang, *Nat. Photonics*, 2018, **12**, 131–142.
24 Q. An, J. Wang, X. Ma, J. Gao, Z. Hu, B. Liu, H. Sun, X. Guo, X. Zhang and F. Zhang, *Energy Environ. Sci.*, 2020, **13**, 5039–5047.
25 M. Gruber, J. Wagner, K. Klein, U. Hörmann, A. Opitz, M. Stutzmann and W. Brütting, *Adv. Energy Mater.*, 2012, **2**, 1100–1108.
26 Y. Shi, Y. Chang, K. Lu, Z. Chen, J. Zhang, Y. Yan, D. Qiu, Y. Liu, M. A. Adil, W. Ma, X. Hao, L. Zhu and Z. Wei, *Nat. Commun.*, 2022, **13**, 3256.
27 J.-L. Wu, F.-C. Chen, Y.-S. Hsiao, F.-C. Chien, P. Chen, C.-H. Kuo, M. H. Huang and C.-S. Hsu, *ACS Nano*, 2011, **5**, 959–967.
28 D. He, M. Zeng, Z. Zhang, Y. Bai, G. Xing, H.-M. Cheng and Y. Lin, *SmartMat*, 2023, e1176.
29 M. Lenes, M. Morana, C. J. Brabec and P. W. M. Blom, *Adv. Funct. Mater.*, 2009, **19**, 1106–1111.
30 L. J. A. Koster, V. D. Mihailetchi, R. Ramaker and P. W. M. Blom, *Appl. Phys. Lett.*, 2005, **86**, 123509.
31 S. Zeiske, O. J. Sandberg, N. Zarrabi, W. Li, P. Meredith and A. Armin, *Nat. Commun.*, 2021, **12**, 3603.
32 P. Bi, S. Zhang, Z. Chen, Y. Xu, Y. Cui, T. Zhang, J. Ren, J. Qin, L. Hong, X. Hao and J. Hou, *Joule*, 2021, **5**, 2408–2419.
33 X. Zhang, L. Qin, J. Yu, Y. Li, Y. Wei, X. Liu, X. Lu, F. Gao and H. Huang, *Angew. Chem., Int. Ed.*, 2021, **60**, 12475–12481.
34 G. Zhang, K. Zhang, Q. Yin, X.-F. Jiang, Z. Wang, J. Xin, W. Ma, H. Yan, F. Huang and Y. Cao, *J. Am. Chem. Soc.*, 2017, **139**, 2387–2395.
35 H. R. Bai, Q. An, M. Jiang, H. S. Ryu, J. Yang, X. J. Zhou, H. F. Zhi, C. Yang, X. Li, H. Y. Woo and J. L. Wang, *Adv. Funct. Mater.*, 2022, **32**, 2200807.

36 J. Yao, T. Kirchartz, M. S. Vezie, M. A. Faist, W. Gong, Z. He, H. Wu, J. Troughton, T. Watson, D. Bryant and J. Nelson, *Phys. Rev. Appl.*, 2015, **4**, 014020.
37 U. Rau, *Phys. Rev. B: Condens. Matter Mater. Phys.*, 2007, **76**, 085303.
38 D. He, F. W. Zhao, C. R. Wang and Y. Z. Lin, *Adv. Funct. Mater.*, 2022, **32**, 2111855.
39 S. Liu, J. Yuan, W. Deng, M. Luo, Y. Xie, Q. Liang, Y. Zou, Z. He, H. Wu and Y. Cao, *Nat. Photonics*, 2020, **14**, 300–305.
40 X.-K. Chen, D. Qian, Y. Wang, T. Kirchartz, W. Tress, H. Yao, J. Yuan, M. Hülsbeck, M. Zhang, Y. Zou, Y. Sun, Y. Li, J. Hou, O. Inganäs, V. Coropceanu, J.-L. Bredas and F. Gao, *Nat. Energy*, 2021, **6**, 799–806.
41 R. A. Marcus, *J. Phys. Chem.*, 1989, **93**, 3078–3086.
42 D. Qian, Z. Zheng, H. Yao, W. Tress, T. R. Hopper, S. Chen, S. Li, J. Liu, S. Chen, J. Zhang, X.-K. Liu, B. Gao, L. Ouyang, Y. Jin, G. Pozina, I. A. Buyanova, W. M. Chen, O. Inganäs, V. Coropceanu, J.-L. Bredas, H. Yan, J. Hou, F. Zhang, A. A. Bakulin and F. Gao, *Nat. Mater.*, 2018, **17**, 703–709.
43 V. Coropceanu, X.-K. Chen, T. Wang, Z. Zheng and J.-L. Brédas, *Nat. Rev. Mater.*, 2019, **4**, 689–707.
44 L. Ye, W. Zhao, S. Li, S. Mukherjee, J. H. Carpenter, O. Awartani, X. Jiao, J. Hou and H. Ade, *Adv. Energy Mater.*, 2017, **7**, 1602000.
45 L. Ye, H. Hu, M. Ghasemi, T. Wang, B. A. Collins, J.-H. Kim, K. Jiang, J. H. Carpenter, H. Li, Z. Li, T. McAfee, J. Zhao, X. Chen, J. L. Y. Lai, T. Ma, J.-L. Bredas, H. Yan and H. Ade, *Nat. Mater.*, 2018, **17**, 253–260.
46 M. Ghasemi, N. Balar, Z. Peng, H. Hu, Y. Qin, T. Kim, J. J. Rech, M. Bidwell, W. Mask, I. McCulloch, W. You, A. Amassian, C. Risko, B. T. O'Connor and H. Ade, *Nat. Mater.*, 2021, **20**, 525–532.
47 M. Sumita, K. Sakata, S. Asai, K. Miyasaka and H. Nakagawa, *Polym. Bull.*, 1991, **25**, 265–271.